Supplementary information

Dynamic self-organization of side-propelling colloidal rods: experiments and simulations

Hanumantha Rao Vutukuri[a*], Zdeněk Preisler[b], Thijs H. Besseling[b], Alfons van Blaaderen[b], Marjolein Dijkstra[b*], Wilhelm T. S. Huck[a*]

[a] Institute for Molecules and Materials, Radboud University, 6525 AJ, Nijmegen, The Netherlands

[b] Soft condensed Matter, Debye Institute for Nanomaterials Science, Utrecht University, 3584 CH, The Netherlands

[*]Email: hanumantharaov@gmail.com, m.dijkstra@uu.nl, & W.Huck@science.ru.nl

Supplementary movie captions:

Movie S1: This confocal movie shows formation and dynamics of self-organization of side-propelling rods with aspect ratio (l/d = 4.1) at a fuel concentration of 0.5 *vol%* H_2O_2. The surface area fraction is $\phi_s \approx 0.07$. The movie was acquired at 10 fps and it is played at 30 fps.

Movie S2: This bight field movie shows the clustering behavior of active rods (l/d = 4.1) at the particle concentration of $\phi_s \approx 0.03$ and a fuel concentration of 0.5 *vol%* H_2O_2. The movie shows that the attractions between tips of propelling rods. The movie was acquired at 20 fps and it is played at 40 fps.

Movie S3: This movie shows Brownian Dynamics simulation of the clustering behavior of side-propelling rods with and without added attractions for a fixed activity of rods ($\mathscr{F}_a$ = 2.0). Left: illustrates the particles with attractions. Right: illustrates the particles without attractions. Same parameters are used as in SFigure 8. The surface area fraction matches with the experimental Figure.2.

MSD and MSAD calculations.

We tracked the positions and orientations of the particles from time-lapsed 2D confocal images using the particle-tracking algorithm as developed by Besseling *et al [1]*. We then obtained the trajectories of the center of mass of the rods using the particle tracking programs of Crocker *et al [2]*. To uniquely identify the tip of the (nearly up-down symmetric) rod, it is required that the rotation angle (θ) of individual rods between successive frames should be less than $\pi/2$.

We calculated the mean square displacement (MSD) and the mean square angular displacement (MSD_θ) using the following expressions.

The rotationally averaged MSD is given by

$$\langle \Delta \boldsymbol{r}^2(t) \rangle \equiv \langle [\boldsymbol{r}(t) - \boldsymbol{r}(0)]^2 \rangle = 4\, D_t\, t + 4\, \epsilon_t^2$$

with D_t the rotationally averaged translational diffusion coefficient and ϵ_t the error in measurement of each of the coordinates of the particle [3]. Next, we projected the particle displacements from the laboratory frame to the body frame using the following expressions [4,5]

$$\begin{pmatrix} \Delta a_n \\ \Delta b_n \end{pmatrix} = \begin{pmatrix} \cos\theta_n & \sin\theta_n \\ -\sin\theta_n & \cos\theta_n \end{pmatrix} \begin{pmatrix} \Delta x_n \\ \Delta y_n \end{pmatrix}$$

where $(\Delta x_n, \Delta y_n)$ is the displacements between the *n*th and (*n*-1)th frame in the laboratory frame, and $(\Delta a_n, \Delta b_n)$ is the corresponding displacements in the body frame. From the body frame trajectories, we calculated the MSDs along the major axis and the minor axes.

$$\langle \Delta \boldsymbol{r}_\parallel^2(t) \rangle \equiv \langle [\boldsymbol{r}_\parallel(t) - \boldsymbol{r}_\parallel(0)]^2 \rangle = 2\, D_\parallel\, t + 2\, \epsilon_\parallel^2$$

$$\langle \Delta \boldsymbol{r}_\perp^2(t) \rangle \equiv \langle [\boldsymbol{r}_\perp(t) - \boldsymbol{r}_\perp(0)]^2 \rangle = 2\, D_\perp\, t + 2\, \epsilon_\perp^2$$

$$D_t = 1/2\ (D_\parallel + D_\perp)$$

where $D_\parallel$ is the diffusion coefficient parallel to the major axis of the rod, and $D_\perp$ is the diffusion coefficient perpendicular to the major axis of the rod.

For the MSD_θ calculations the following expression is used

$$\langle \Delta\theta^2(t) \rangle = 2\, D_r\, t + \epsilon_r^2$$

where D_r is the rotational diffusion coefficient.

We extended previous models [6,7] on active diffusion of self-propelled spherical particles to our active rods by taking into account the shape anisotropy. In the short-time limit $\Delta t \ll \tau_R$, the MSD for active particles is given by [6,8,9]

$$\langle \Delta \boldsymbol{r}^2(t) \rangle \equiv \langle [\boldsymbol{r}(t) - \boldsymbol{r}(0)]^2 \rangle = 4\, D_t\, t + v^2 t^2 + 4\, \epsilon_t^2$$

where v is the propulsion speed, and τ_R is the rotational diffusion time. We projected these displacements to the body frame

$$\langle \Delta \boldsymbol{r}_{\parallel}^2(t) \rangle \equiv \langle [\boldsymbol{r}_{\parallel}(t) - \boldsymbol{r}_{\parallel}(0)]^2 \rangle = 2\, D_{\parallel}\, t + v_{\parallel}^2 t^2 + 2\, \epsilon_{\parallel}^2$$

$$\langle \Delta \boldsymbol{r}_{\perp}^2(t) \rangle \equiv \langle [\boldsymbol{r}_{\perp}(t) - \boldsymbol{r}_{\perp}(0)]^2 \rangle = 2\, D_{\perp}\, t + v_{\perp}^2 t^2 + 2\, \epsilon_{\perp}^2$$

such that $D_t = 1/2\ (D_{\parallel} + D_{\perp})$ and $v^2 = v_{\parallel}^2 + v_{\perp}^2$.

We calculated the propulsion velocities by fitting the MSDs with the above mentioned equations. In the long-time limit $\Delta t \gg \tau_R$, rotational diffusion randomizes the propulsion direction that leads to diffusive like behavior with an effective diffusion coefficient.

$$D_{prop,\perp} = D_{eq,\perp} + (1/2)\, v_{\perp}^2\, \tau_R$$

$$D_{prop,\parallel} = D_{eq,\parallel} + (1/2)\, v_{\parallel}^2\, \tau_R$$

where $v_{\parallel}$ is the propulsion velocity parallel to the major axis of the rod, and $v_{\perp}$ is the propulsion velocity perpendicular to the major axis of the rod.

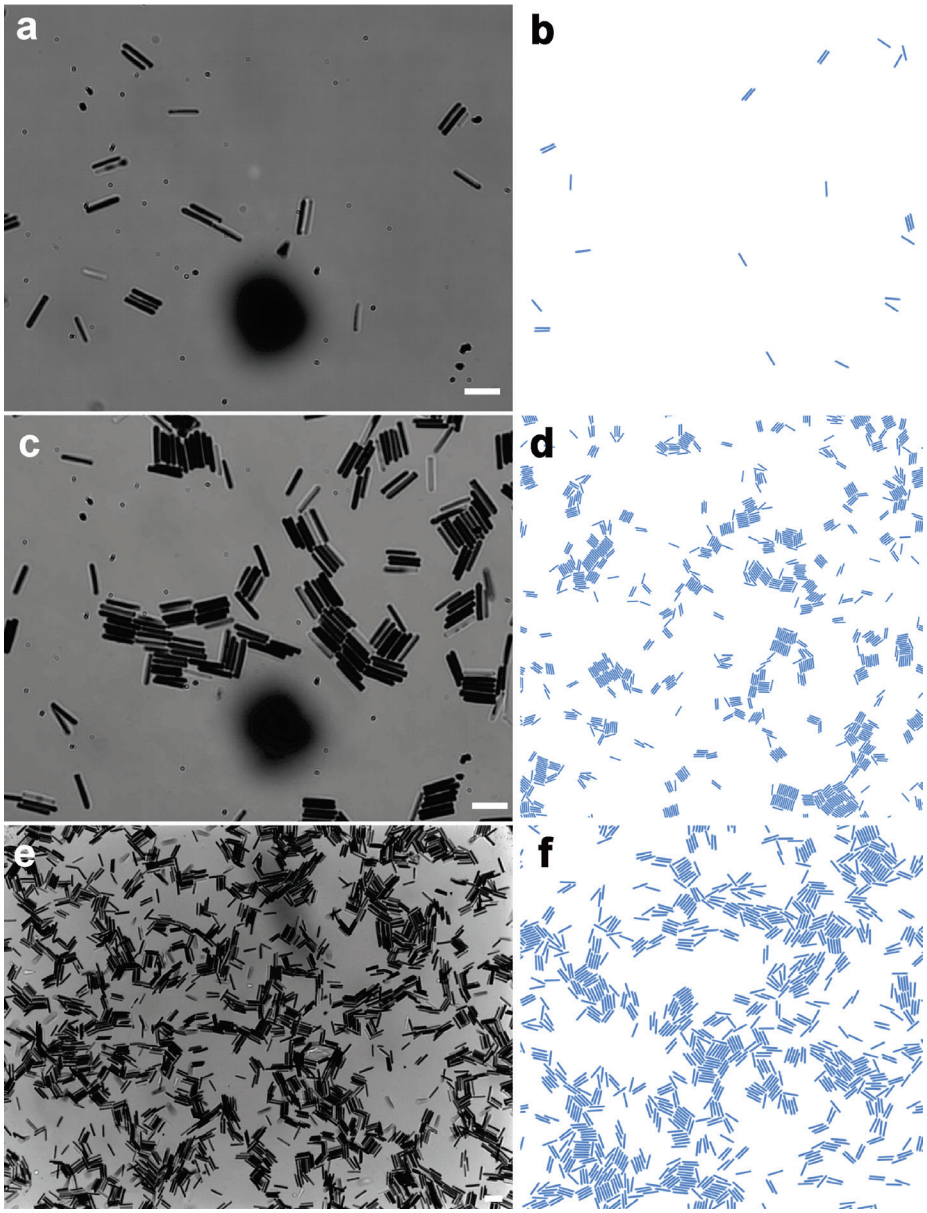

SFigure 1. Experimental and simulation results on dynamic self-organization of Janus rods (*l/d* = 7) as a function of particle concentration ϕ_s at the fuel concentration of 0.5 *vol%* H_2O_2. (**a**) Mainly doublets, occasionally triplets at very dilute concentration, $\phi_s \approx 0.01$. (**c**) Small clusters of active rods at dilute particle concentrations, $\phi_s \approx 0.09$. (**e**) Big clusters of rods at moderate particle concentrations $\phi_s \approx 0.30$. (**b, d, f**) Snapshots from the simulations for the corresponding concentrations. The parameters used: **(b)** activity $\mathscr{P}_a = 1.5$, and attraction strengths $\beta\lambda_1 = 1.5$, **(d)** $\mathscr{P}_a = 1.5$, and $\beta\lambda_1 = 2.0$, and **(f)** $\mathscr{P}_a = 1.5$, and $\beta\lambda_1 = 1.0$. The scale bar is 5.0 μm.

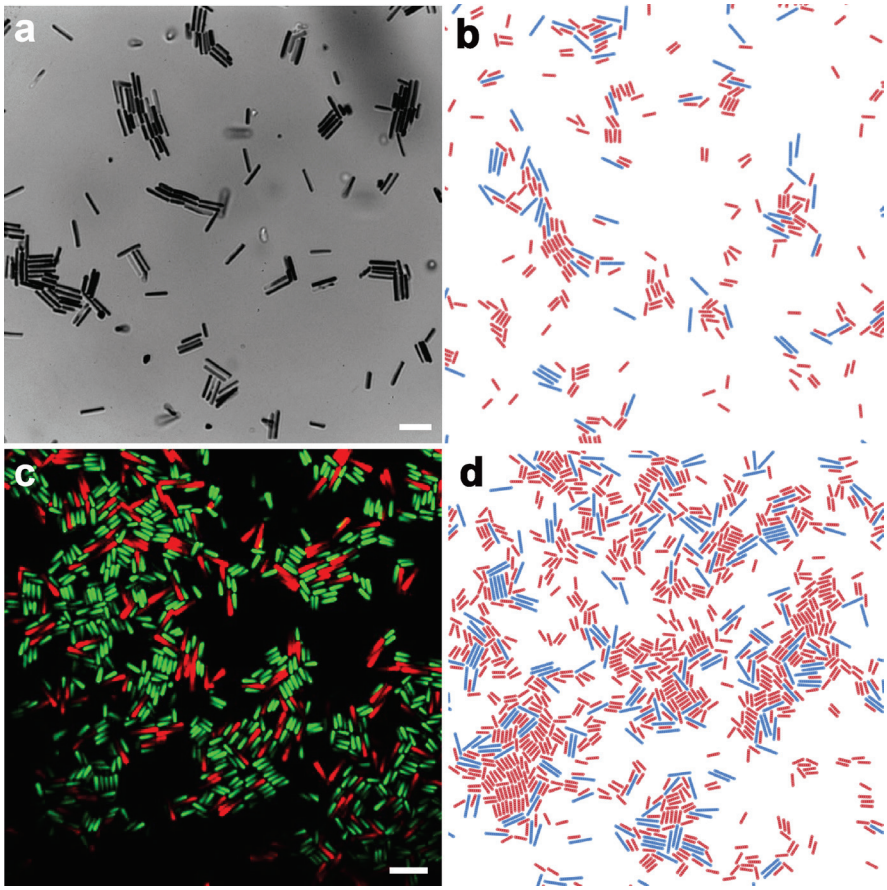

SFigure 2. Active clusters of binary mixtures of rods with different sizes of rods in 0.5 *vol%* H_2O_2 solution. (**a**) $\phi_s \approx 0.08$. (**c**) $\phi_s \approx 0.25$. Particles with aspect ratio 4.1 are color coded with green, and the aspect ratio 7 rods are color coded with red. (**b, d**) Simulation snapshots for the corresponding concentrations. Blue represents the long rods, and red represents the short rods. The parameters used: **(b)** activity $\mathscr{T}_a = 1.5$, and attraction strengths $\beta\lambda_1 = 1.5$, **(d)** $\mathscr{T}_a = 1.5$, and $\beta\lambda_1 = 1.5$. The scale bar is 5.0 μm.

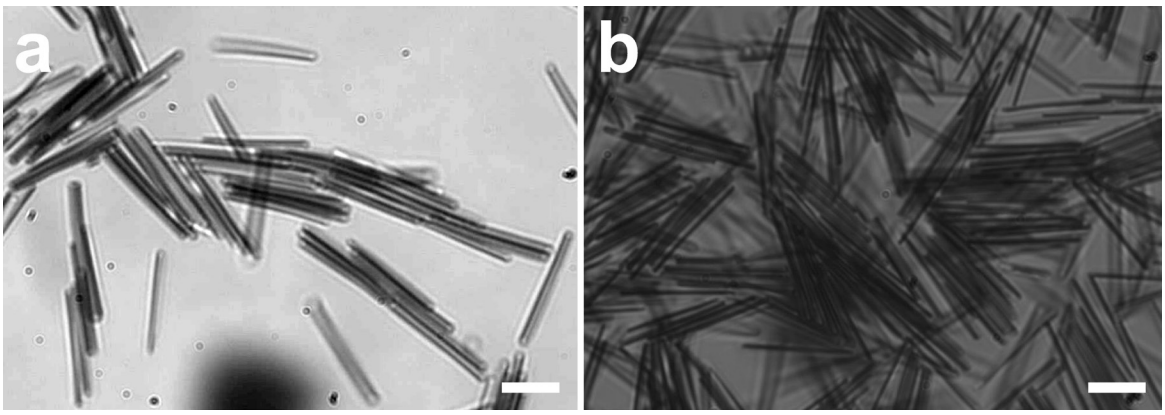

SFigure 3. Bright field images of self-organized longer Janus rods (aspect ratio *l/d* = 20.4) in 0.5 *vol%* H_2O_2 solution. (**a**) Small active clusters of particles at surface area fraction of rods $\phi_s \approx 0.15$. (**b**) System jammed at surface area fraction of rods $\phi_s > 0.25$. Scale bar is 5.0 μm.

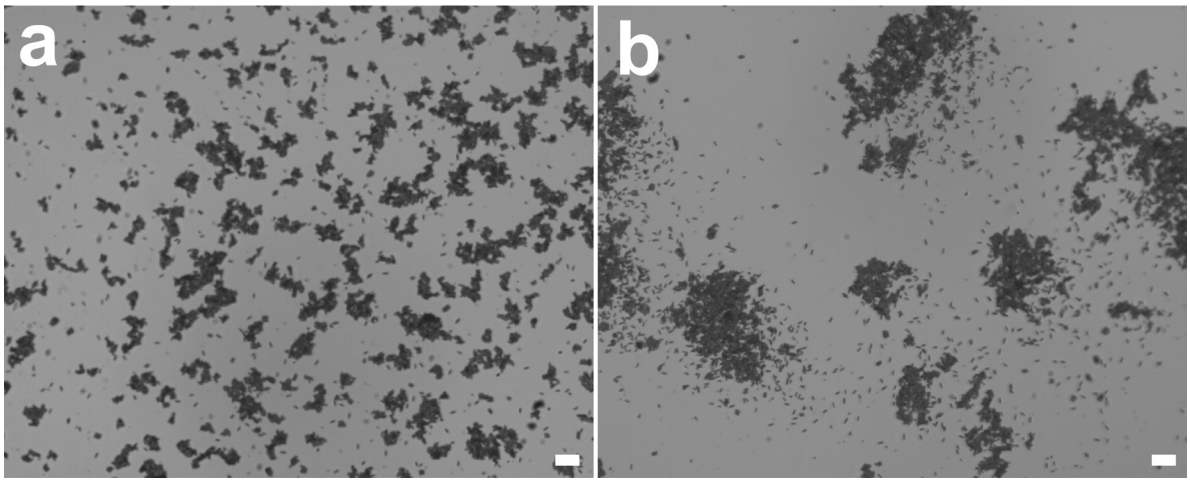

SFigure 4. Time-lapsed bright field images show the structural evolution of the phase separation of the rods at a higher density. The time difference between the two images was about 10 mins. The scale bar is 20.0 μm.

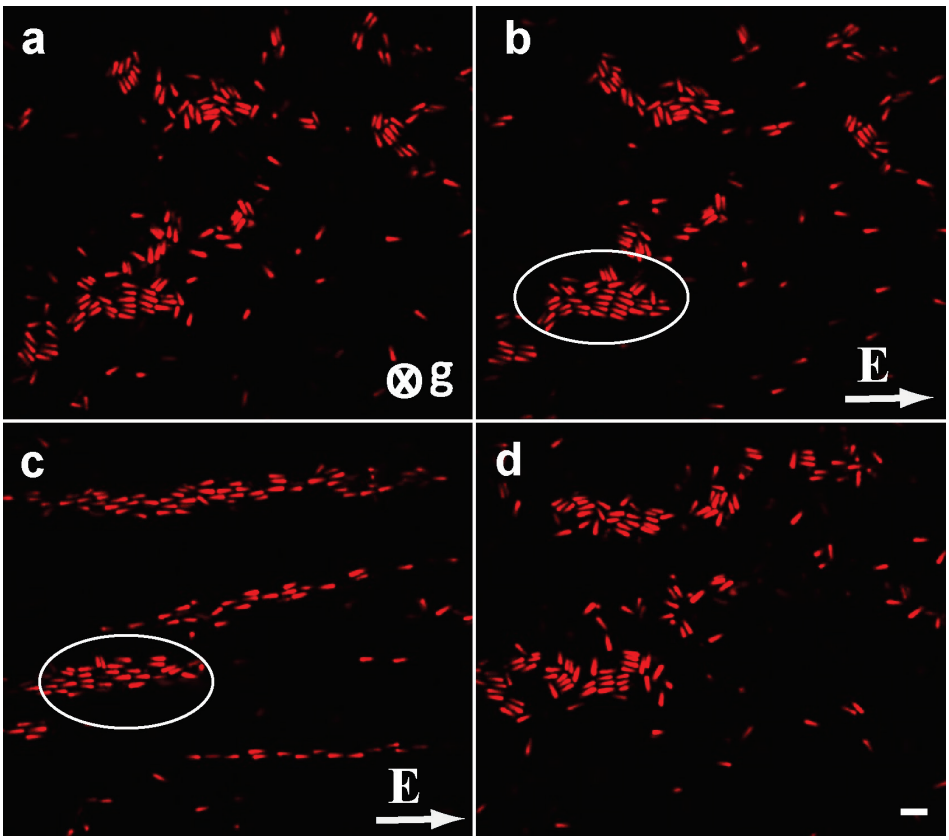

SFigure 5. Confocal micrographs show the response of clusters of active rods in AC electric fields. (**a**) In the absence of the field. (**b**) In the presence of a low AC electric field (E_{rms} = 0.001 Vμm^{-1}, f = 500 kHz). (**c**) Clusters of rods transformed into zig-zag like configuration at a high electric field (E_{rms} = 0.01 Vμm^{-1}, f = 500 kHz). The skewed white ellipse indicates transformation of clusters to zig-zag configuration. (**d**) Shortly after switching off the field. Scale bars are 3.0 μm.

Active clusters in external AC electric fields

We constructed an electric cell from a no. 1 glass cover slip (130-160 μm thick, Menzel) onto which two coplanar electrodes were fabricated by sputter coating with 3 nm chromium followed by 20 nm of gold (Cressington 208hr). The distance between two gold electrodes was 4 mm. A 10 μl droplet suspension of the active rods was placed between the electrodes and it was made sure that there was contact with the both electrodes. For electrical contacts with gold electrodes we used silver paint (Jeol) and thin thermocouple alloy wire (diameter of 50 μm, Good fellow), which was then wrapped around standard electronic wire. A function generator (Agilent, Model

3312 OA) and a wide band voltage amplifier (Krohn-Hite, Model 7602M) were used to generate the electric fields. The field strength and the frequency were measured using an oscilloscope (Tektronix, Model TDS3052).

Brownian Dynamics Simulations

We simulated N rigid rods of length L and dimater σ with periodic boundary conditions. The aspect ratio is defined as L/σ. We mimic each colloidal rod by n segments equidistantly aligned on a line [10], where each segment is described by a pair potential. The total interaction of two rods is the sum of all the segment-segment interactions between the two rods.

The interaction between two rods k and l reads

$$U_{rod}^{(k,l)} = \sum_{i=1}^{n}\sum_{j=1}^{n} U_{seg}\left(q_{ij}^{(k,l)}\right).$$

The distance between two segments i and j is given by $\left|\boldsymbol{q}_i^{(k)} - \boldsymbol{q}_j^{(l)}\right|$, where $\boldsymbol{q}_i^{(k)}$ denotes the position of segment i of rod k and U_{seg} is the interaction potential between two segments (see **SFig. 6**).

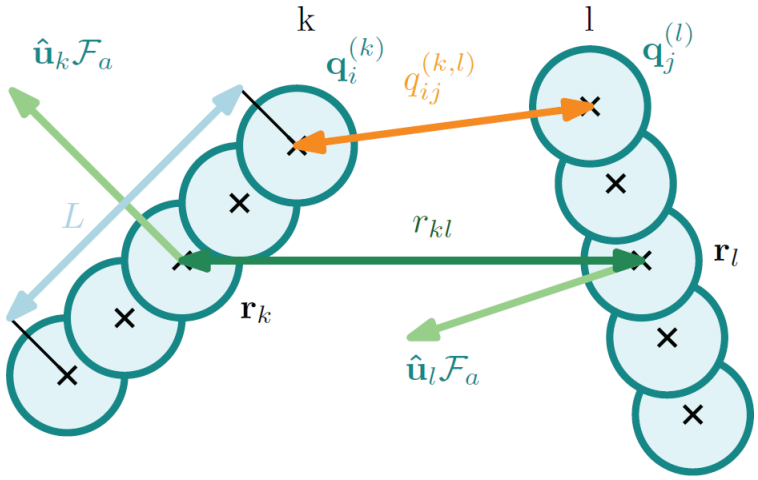

SFigure 6. Schematic representation of the interaction between rods *k,* and *l.*

We then write the segment-segment interaction potential in the following fashion in order to add the attractive tail to our model

$$\beta \bigcup_{seg}(\epsilon, \lambda, q_{ij}) = \begin{cases} \beta\epsilon \bigcup_{LJ}(q_{ij}) + \beta(\lambda - \epsilon) \bigcup_{LJ}(d), & q_{ij} \leq d \\ \beta\lambda \bigcup_{LJ}(q_{ij}), & q_{ij} > d \end{cases} \quad (1)$$

where ϵ is the repulsion strength, λ corresponds to the strength of the attraction, $\beta = \frac{1}{k_B T}$ is the inverse temperature with k_BBoltzmann's constant, and $d = 2^{1/6}\,\sigma$ is the minimum of the Lennard-Jones (LJ) potential. $\bigcup_{LJ}(q_{ij})$ stands for the LJ interaction potential

$$\bigcup_{LJ}(q_{ij}) = 4\left[\left(\frac{\sigma}{q_{ij}}\right)^{12} - \left(\frac{\sigma}{q_{ij}}\right)^{6}\right]$$

where σ is our unit of length. Note that for $\lambda = 0$, we recover the Weeks-Chandler-Andersen potential.

The attraction observed in the experiments appears to be anisotropic. In particular, we observed a stronger attraction between the tips of the rods. We included this behavior in our model by changing the interaction between the end segments. We further generalized the segment-segment interaction potential, Eq., 1 in the following way

$\lambda = \lambda_1$ if *i*= 1 or *n* and *j*= 1 or *n*

$\lambda = \lambda_2$ otherwise,

where λ_1 is the attraction strength between the end segments and λ_2 is the interaction strength between all other segments. For clarity, the interactions between two rods are depicted in **SFig. 6.**

We employed the following equations of motion for rod *k*

$$\frac{d}{dt}\,\boldsymbol{r}_k(t) = \frac{\boldsymbol{F}_k(t)}{\boldsymbol{f}_T} + \sqrt{\frac{2\,k_B T}{\boldsymbol{f}_T}}\,\boldsymbol{\xi}_k(t) + \hat{\boldsymbol{u}}_k(t)\,\frac{F_a}{\boldsymbol{f}_T},$$

where $\boldsymbol{r}_k(t)$ is the center of mass of rod *k* at time *t*, $\boldsymbol{F}_k(t) = -\nabla_{r_k}\sum_{l=1,l\neq k}^{n}\bigcup_{rod}^{(k,l)}$ is the force on rod *k* due to the particle interactions with all other rods, $\boldsymbol{f}_T$ denotes the translational friction tensor, $\boldsymbol{\xi}_k(t)$ is a stochastic force with zero mean that describes the collisions with the solvent molecules, *T* denotes the temperature of the Brownian bath, and satisfies $< \boldsymbol{\xi}_k(t)\boldsymbol{\xi}_l(t') > = \delta_{kl}\delta(t - t')$, and F_a is a constant self-propulsion force acting perpendicular to the major axis of the rod i.e. in the direction of $\hat{\boldsymbol{u}}_k(t)$ at time t. The equation of motion for the orientation of the rod *k* reads

$$\frac{d}{dt}\,\hat{\boldsymbol{u}}_k(t) = \frac{\boldsymbol{T}_k(t)}{\boldsymbol{f}_R} + \sqrt{\frac{2\,k_B T}{\boldsymbol{f}_R}}\,\boldsymbol{\xi}_k(t)$$

where $\nabla_{\hat{\boldsymbol{u}}} \bigcup_{rod}(\boldsymbol{r}_k)\ \boldsymbol{T}_k(t) = -\nabla_{\hat{\boldsymbol{u}}_k} \sum_{l=1, l\neq k}^{n} \bigcup_{rod}^{(k,l)}$ corresponds to the torque acting on rod k due to the presence of all other rods, $\boldsymbol{f}_R$ denotes the rotational friction tensor, $\boldsymbol{\xi}_k(t)$ is a white noise. Further, we denote the translational and rotational friction tensors respectively as

$$\boldsymbol{f}_T = \gamma_0[f_{\parallel}\hat{\boldsymbol{u}}_k\,\hat{\boldsymbol{u}}_k + f_{\perp}(\mathbf{I} - \hat{\boldsymbol{u}}_k\,\hat{\boldsymbol{u}}_k)\,]$$

$$\boldsymbol{f}_R = \gamma_0 f_R \mathbf{I}$$

where $\mathbf{I}$ is the 2D unit tensor, $f_{\parallel}, f_{\perp}$, f_R are dimensionless the translational and rotational friction coefficients, and γ_0 the Stokesian friction coefficient.

Friction coefficients

The friction coefficients are taken from Tirado et al. [11] The coefficients read

$$\frac{2\pi}{f_{\parallel}} = \ln a - 0.207 + \frac{0.980}{a} - \frac{0.133}{a^2}$$

$$\frac{4\pi}{f_{\perp}} = \ln a + 0.839 + \frac{0.185}{a} + \frac{0.233}{a^2}$$

$$\frac{\pi\,a^2\sigma^2}{3\,f_R} = \ln a - 0.662 + \frac{0.917}{a} - \frac{0.050}{a^2}$$

With $a = L/\sigma$ the aspect ratio of the rods. For convenience we define an effective propulsion force that we vary in our simulations as follows

$$\mathscr{F}_a = \frac{F_a\,\sigma}{f_{\perp}\,k_B T}$$

The Euler-Maruyama method is used to integrate the above described stochastic differential equations.

Adaptive time-step algorithm

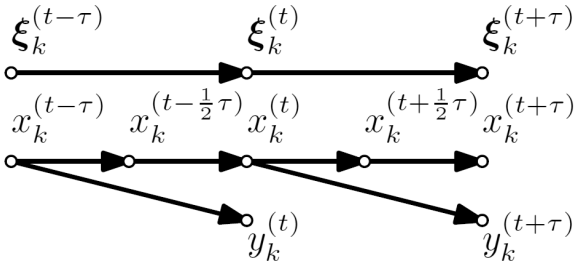

SFigure 7. Integration along a fixed Brownian path $\boldsymbol{\xi}_k(t)$ with two time steps τ and $\tau/2$, denoted by the phase space trajectory $\ldots, x_k(t-\tau), x_k(t-\tau/2), x_k(t), x_k(t+\tau/2), x_k(t+\tau), \ldots$ and $\ldots, x_k(t-\tau), y_k(t), y(t+\tau), \ldots$, respectively. The error of the trajectory of the *k*-th particle at time *t* is estimated as the distance $\varepsilon_k(t) \equiv |x_k(t) - y_k(t)|$.

Effectively simulating a self-propelled Brownian system is a surprisingly challenging task. In particular, it can become tedious to set an appropriate time step in our simulations. To integrate properly, the time step has to be just right i.e. not too small and not too large either. A too small time step results in an inefficient simulation, while a too large time step results in an inaccurate integration. Our case, is further complicated by the presence of the active force. The propulsion induces more overlaps of the particles, in other words, the potential energy due to the particle interactions increases significantly. Note that the error of the stochastic differential equations does not scale the same way as in the case of the ordinary differential equations, and a more careful approach is needed due to the random noise.

To bypass this difficulty, we propose the following method, which is based on estimating the integration error along a fixed Brownian path. The time-step is varied according to the estimated error during the simulation.

The error, ε, is estimated by carrying out the integration with two different time steps (τ, $\tau/2$) along a stochastic trajectory $\xi(t)$ denoted by the phase space trajectory $\ldots, x_k(t-\tau), x_k(t-\tau/2), x_k(t), x_k(t+\tau/2), x_k(t+\tau), \ldots$ and $\ldots, x_k(t-\tau), y_k(t), y(t+\tau), \ldots$, respectively. Hence, two phase points *x(t), y(t)* are generated at time *t*, where $x \equiv (r_{1,} \ldots\ldots, r_{2n}, u_{1,} \ldots\ldots, u_{2n})$. We estimate the error as a distance between these two phase points $\varepsilon(t) \equiv |x(t) - y(t)|$. In our case we define the distance $|x_k(t) - y_k(t)|$ as an Euclidean distance between the centers of mass of the rods $\varepsilon_k(t) \equiv \left|\boldsymbol{r}_k{}^{\tau/2}(t) - \boldsymbol{r}_k^{\tau}(t)\right|$. We vary the time-step τ at time *t* using the error estimate calculated at the previous integration step $\varepsilon_{max}(t-1)$. If the previous integration had

an error larger than a given threshold ($\varepsilon_{max} > \varsigma_{max}$), we decrease the following time-step and vice versa if the integration is too refined ($\varepsilon_{max} < \varsigma_{max}$) we increase the integration time-step. The above described scheme allowed us to set our integration precision rather than defining fixed τ for every simulation.

We performed Brownian dynamics simulations of colloidal rods with a self-propulsion force in the direction perpendicular to the major axis as described above in detail. All simulations are first equilibrated in the absence of the self-propulsion force. We set the Brownian bath temperature kT as our unit of energy, the interaction strength $\beta\epsilon$ = 10, and $\beta\lambda_2$= 0.1 $\beta\lambda_1$.

We calculated rods with the aspect ratios L/σ = 4 with number of segments n=6 and L/σ =7 with n =11. In all cases we simulated systems with fixed number of particles N = 1024. First we calculate purely repulsive systems i.e. $\lambda = 0$. We then simulated systems for various parameters changing the propulsion strength $\mathscr{F}_a$ and attraction strength λ_1, λ_2 for various number densities and aspect ratios. We simulated the state behavior of side-propelled rods for wide range of activities, attraction strengths, and number densities. However, we of only present a selected data set. For rods with aspect ratio L/σ = 4, the resulted state behavior is depicted in **SFigs. 8-10**. For aspect ratio L/σ = 7.0, the resulted state behavior is shown in **SFigs. 11-12**. Moreover, we also simulated the binary mixtures of rods with aspect ratios L/σ = 4.0 and 7.0.

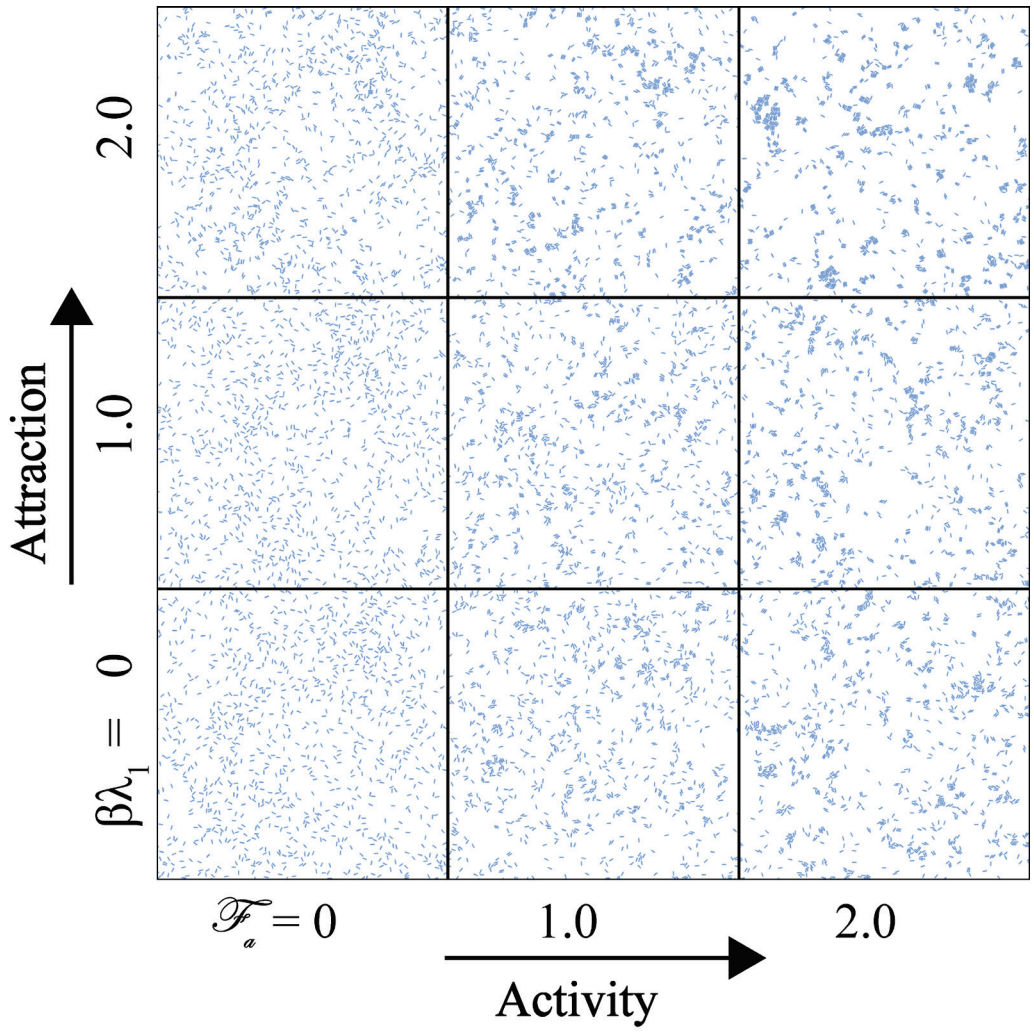

SFigure 8. Simulation snapshots illustrate the state behavior of side-propelled rods with aspect ratio of L/σ = 4.0 for different activities $\mathscr{F}_a$, and attraction strengths $\beta\lambda_1$ for fixed number of rods N=1024, number density $\rho\ \sigma^2$= 0.018, repulsion strength $\beta\epsilon$ =10, and $\beta\lambda_2$= 0.1 $\beta\lambda_1$.

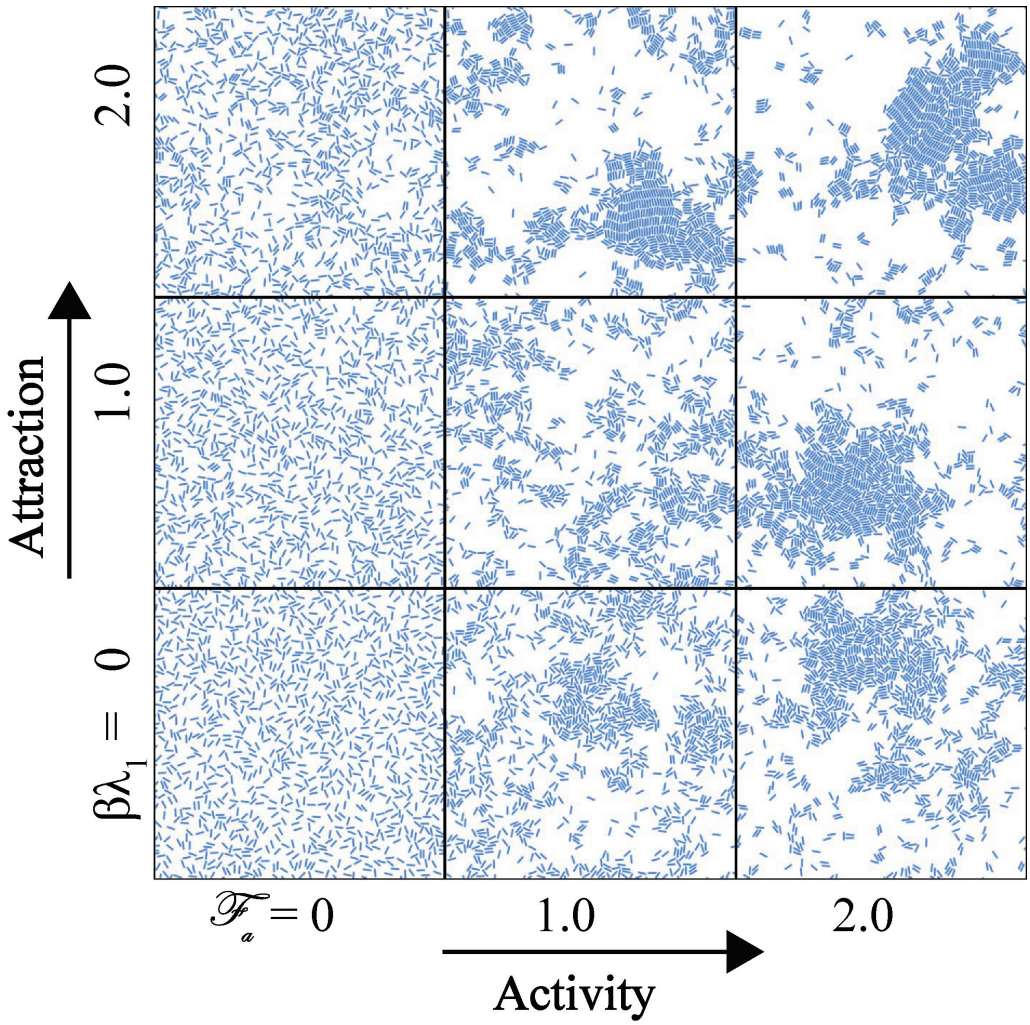

SFigure 9. Simulation snapshots illustrate the state behavior of side-propelled rods with aspect ratio L/σ = 4.0 for different activities $\mathscr{F}_a$, and attraction strengths $\beta\lambda_1$ for fixed number of rods N=1024, repulsion strength $\beta\epsilon$ =10, and $\lambda\beta_2$= 0.1 $\beta\lambda_1$, and a higher number density $\rho\ \sigma^2$= 0.065 than in SFigure 8.

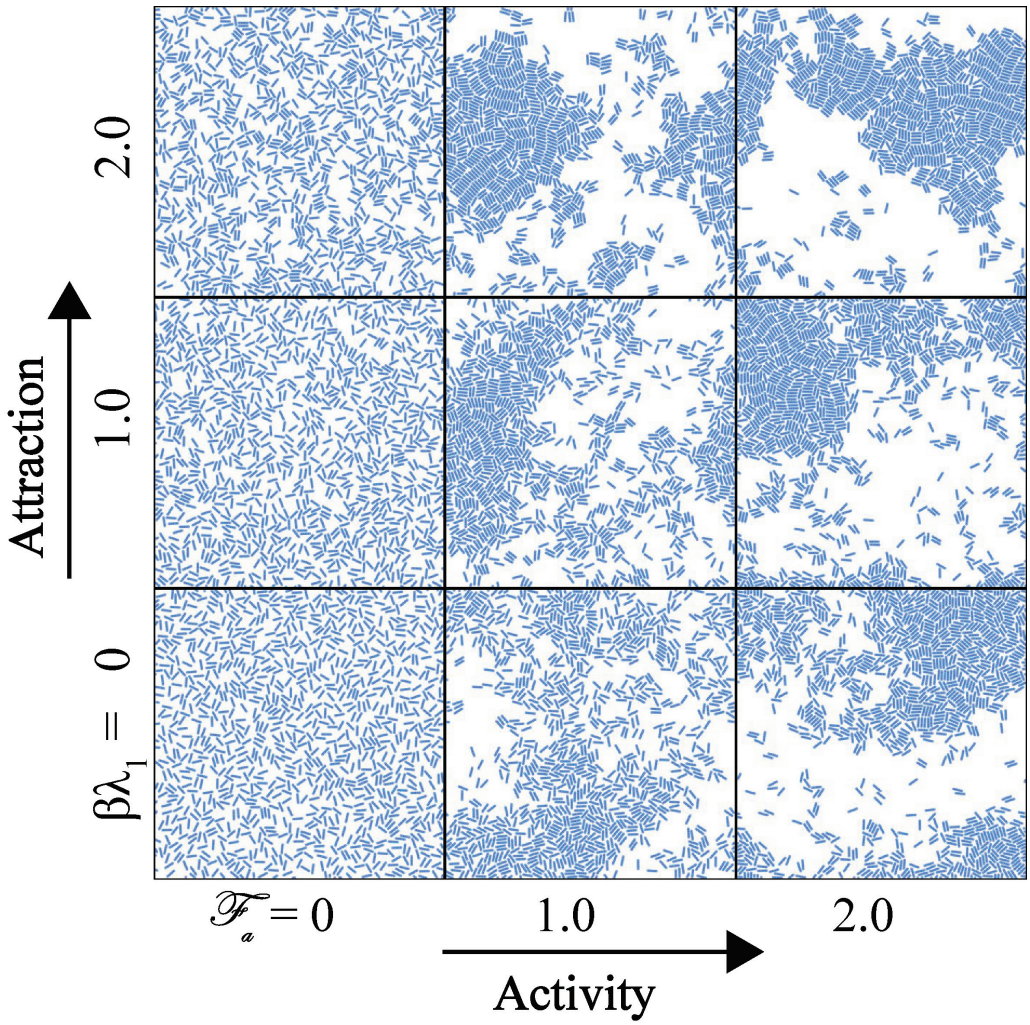

SFigure 10. Simulation snapshots illustrate the state behavior of side-propelled rods with aspect ratio L/σ = 4.0 for different activities $\mathscr{F}_a$, and attraction strengths $\beta\lambda_1$ for fixed number of rods N=1024, repulsion strength $\beta\epsilon$ =10, and $\beta\lambda_2$= 0.1 $\beta\lambda_1$, and a higher number density $\rho\ \sigma^2$= 0.097 than in SFigure 9.

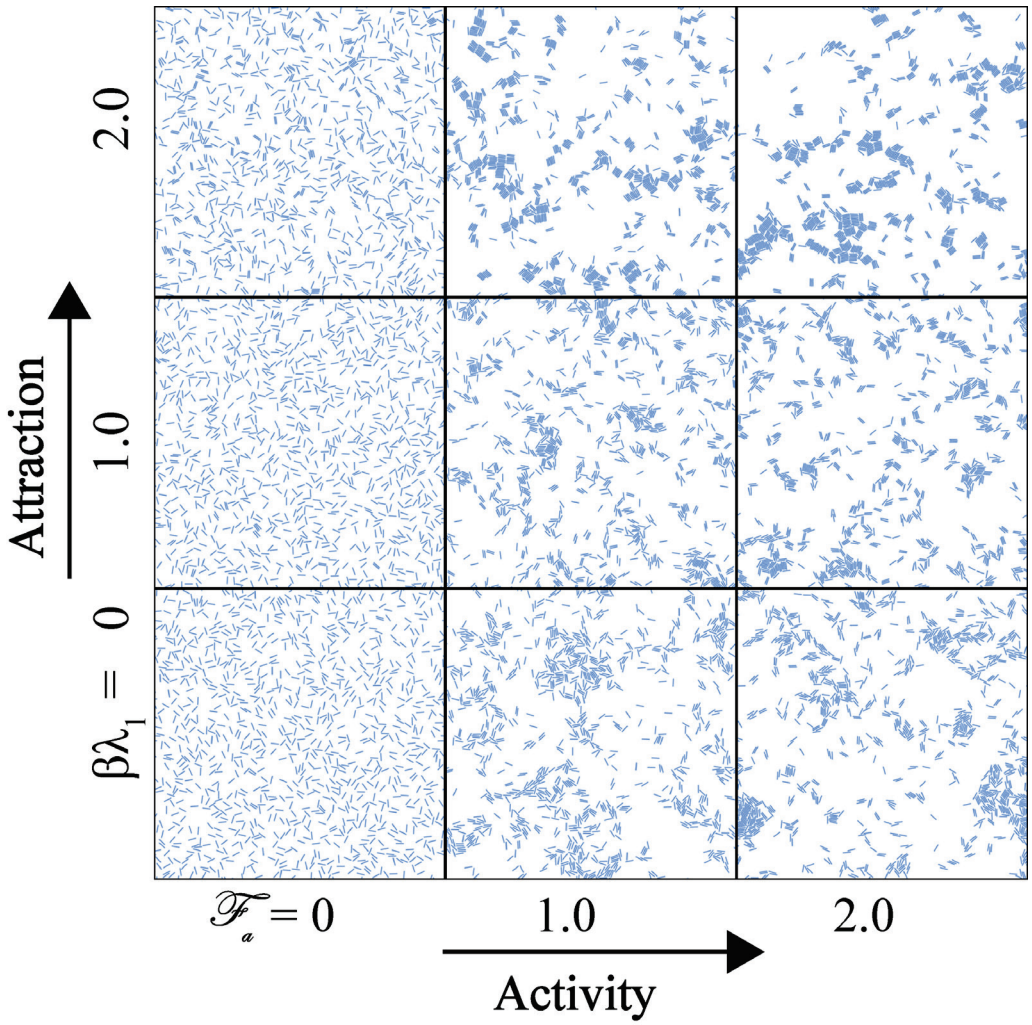

SFigure 11. Simulation snapshots illustrate the state behavior of side-propelled rods with a larger aspect ratio L/σ = 7.0 than in SFigure 8, 9, and 10 for different activities $\mathscr{F}_a$, and attraction strengths $\beta\lambda_1$ for fixed number of rods N=1024, number density $\rho\,\sigma^2$= 0.018, repulsion strength $\beta\epsilon$ =10, and $\beta\lambda_2$= 0.1 $\beta\lambda_1$.

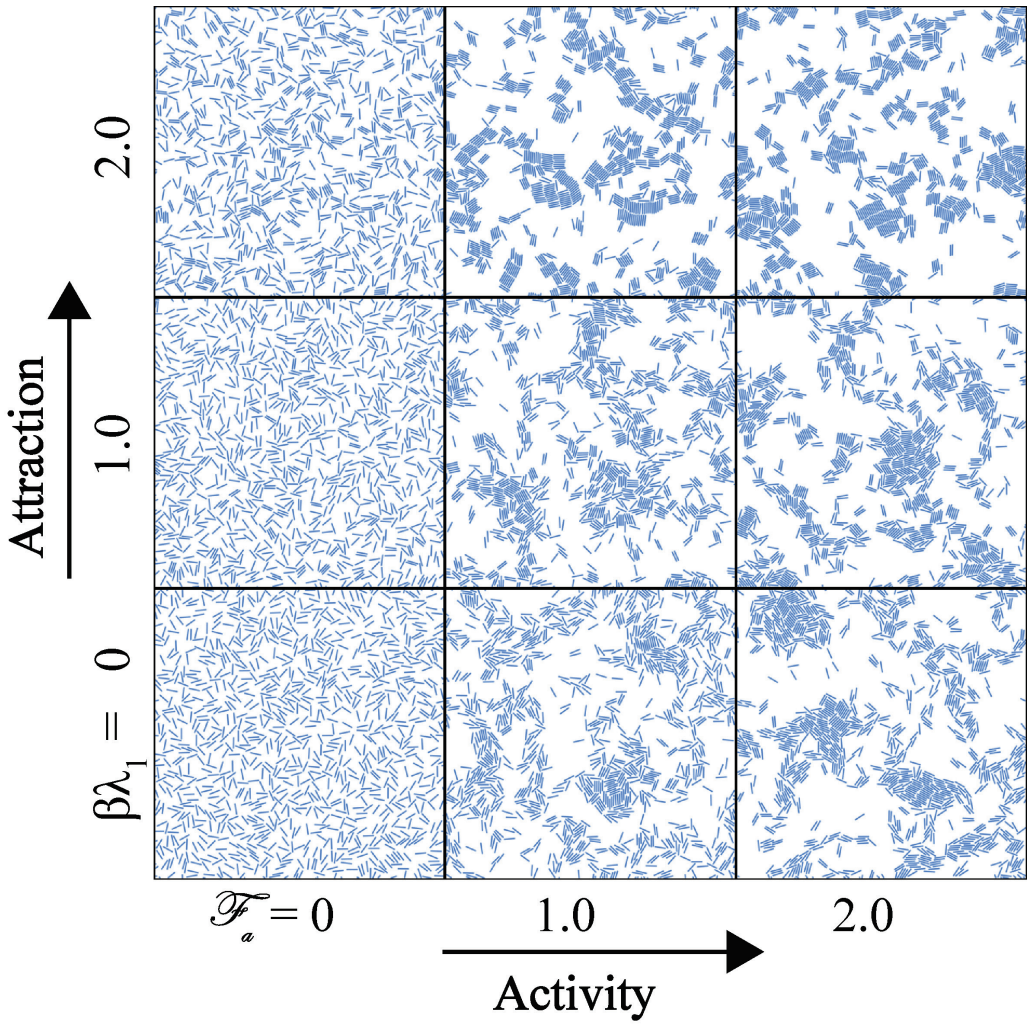

SFigure 12. Simulation snapshots illustrate the state behavior of side-propelled rods with aspect ratio L/σ = 7.0 for different activities $\mathscr{F}_a$, and attraction strengths $\beta\lambda_1$ for fixed number of rods N=1024, number density $\rho\ \sigma^2$= 0.035, repulsion strength $\beta\epsilon$ =10, and $\beta\lambda_2$= 0.1 $\beta\lambda_1$.

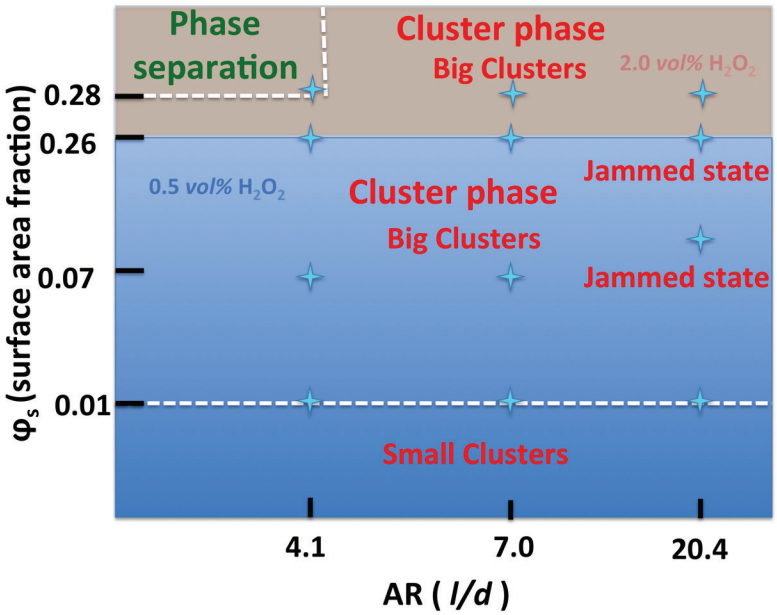

SFigure 13. This diagram summarizes the observed phases for a combination of aspect ratio (AR) of the rods and surface area fractions for different activities (i.e. 0.5, 2.0 *vol%*). Note that the blue color represents the 0.5 *vol%* and the light grey color represents the 2.0 *vol%* H_2O_2, respectively. Across symbols denote the experimental points that are supported by simulation predictions.

References:

[1] T. H. Besseling, M. Hermes, A. Kuijk, B. de Nijs, T. S. Deng, M. Dijkstra, A. Imhof, and A. van Blaaderen, J Phys-Condens Mat **27** (2015).
[2] J. C. Crocker and D. G. Grier, Journal of Colloid and Interface Science **179**, 298 (1996).
[3] T. Savin and P. S. Doyle, Biophys J **88**, 623 (2005).
[4] Y. Han, A. Alsayed, M. Nobili, and A. G. Yodh, Phys Rev E Stat Nonlin Soft Matter Phys **80**, 011403 (2009).
[5] Y. Han, A. M. Alsayed, M. Nobili, J. Zhang, T. C. Lubensky, and A. G. Yodh, Science **314**, 626 (2006).
[6] J. R. Howse, R. A. L. Jones, A. J. Ryan, T. Gough, R. Vafabakhsh, and R. Golestanian, Phys Rev Lett **99** (2007).
[7] J. Elgeti, R. G. Winkler, and G. Gompper, Rep Prog Phys **78** (2015).
[8] G. Dunderdale, S. Ebbens, P. Fairclough, and J. Howse, Langmuir **28**, 10997 (2012).
[9] J. Palacci, S. Sacanna, A. P. Steinberg, D. J. Pine, and P. M. Chaikin, Science **339**, 936 (2013).
[10] H. H. Wensink and H. Lowen, J Phys Condens Matter **24**, 464130 (2012).
[11] M. M. Tirado, C. L. Martínez, and J. G. de la Torre, The Journal of Chemical Physics **81**, 2047 (1984).